# Evidence for biogenic graphite in early Archaean Isua metasedimentary rocks

Yoko Ohtomo[1]*, Takeshi Kakegawa[1], Akizumi Ishida[1], Toshiro Nagase[1] and Minik T. Rosing[2]

**Some graphite contained in the 3.7-billion-year-old metasedimentary rocks of the Isua Supracrustal Belt, Western Greenland[1], is depleted in $^{13}C$ and has been interpreted as evidence for early life[2]. However, it is unclear whether this graphite is primary, or was precipitated from metamorphic or igneous fluids[3,4]. Here we analyse the geochemistry and structure of the $^{13}C$- depleted graphite in the Isua schists. Raman spectroscopy and geochemical analyses indicate that the schists are formed from clastic marine sediments that contained $^{13}C$-depleted carbon at the time of their deposition. Transmission electron microscope observations show that graphite in the schist occurs as nanoscale polygonal and tube-like grains, in contrast to abiotic graphite in carbonate veins that exhibits a flaky morphology. Furthermore, the graphite grains in the schist contain distorted crystal structures and disordered stacking of sheets of graphene. The observed morphologies are consistent with pyrolysation and pressurization of structurally heterogeneous organic compounds during metamorphism. We thus conclude that the graphite contained in the Isua metasediments represents traces of early life that flourished in the oceans at least 3.7 billion years ago.**

The suggestion that graphite in early Archaean rocks represents materials of biogenic origin has been met with a degree of scepticism[5,6]. Isotopic compositions of graphite in >3.7-billion-year old (Ga) rocks from the Isua Supracrustal Belt (ISB), Western Greenland, which are believed to be of sedimentary origin, suggest that vast microbial ecosystems were present in early Archaean oceans[7,8]. However, results of more recent studies suggest that most of the graphite-bearing rocks formed through interactions between crustal fluids and surrounding igneous rocks[3,4] during later metasomatic events[9], thereby casting doubt on the existence of an extensive sedimentary sequence in the ISB and on the biogenic origin of constituents. In contrast, $^{13}C$-depleted graphite globules, which are considered to form from biogenic precursors, have been reported from metamorphosed clastic sedimentary rocks in the ISB (ref. 2). However, these globules were found at a single locality, and it therefore remains unclear whether traces of life at other localities in the ISB were lost during metamorphism or were originally absent. The presence of additional clastic sedimentary rocks containing graphite may provide evidence for the preservation of organic constituents in early Archaean rocks, thus supporting the notion that microbes were active in early Archaean oceans.

We conducted a geological survey along the northwestern area of the ISB (Fig. 1a,b), where the rocks are generally less affected by deformation than in other areas of the belt[10]. Metamorphosed basalts and banded iron formations (BIFs) are dominant in this area. The BIFs contain interbedded black to grey schist layers (Fig. 1b–d), typically 40–80 cm thick. The schist mainly comprises chlorite, cummingtonite, quartz and reduced carbon (see Supplementary Fig. 1 and Table 1). The black–grey schist in the northern part of the area contains moderate amounts of Al, Ti and Zr, probably representing detrital components (see Supplementary Information). The rare earth element (REE) patterns (normalized by the composition of post-Archaean Australian shale, PAAS; ref. 11) in the Al-rich rocks (samples 3072303 and 6072905) lie close to the line defined by a rock/PAAS ratio of 1, with the exception of slightly lower ratios for light REEs (Fig. 2). These REE patterns and Al-rich characteristics suggest that the protoliths of the schist were clastic marine sediments. However, some of the examined rocks have compositions resembling those of BIFs (for example, samples 4062308, 4062309 and 5080501).

The black–grey schist samples contain abundant reduced carbon (0.1–8.8 wt%), identified as graphite by X-ray diffraction (XRD) analysis (Supplementary Tables 3 and 4). The graphite-rich schist from the northern part of the area is folded, as are the surrounding BIFs. A sample from this folded area contains the highest concentrations of $C_{graphite}$ (8.8 wt% C) measured in the present study. At other locations, the schist is concordantly intercalated in layers of BIFs, and contains moderate concentrations of $C_{graphite}$ (0.1–0.5 wt% C; Supplementary Table 3). In general, graphite concentrations on microscopic scales vary according to the compositional layering of the schist, which strikes parallel to that of the surrounding BIFs. Thus, the moderate to high $C_{graphite}$ concentrations, the correspondence of $C_{graphite}$ concentrations with compositional layering and the concordant layering of schist and BIF units all support a sedimentary origin of the reduced carbon.

It has been suggested that disproportionation of Fe-carbonate during metamorphism accounts for the genesis of the graphite in secondary carbonate veins[4]. In such veins, substantial amounts of magnetite and residual Fe-carbonate occur along with the graphite. However, Fe-carbonate and magnetite are absent from the graphite-rich schist in this study. Therefore, it is unlikely that the graphite originated from the thermal disproportionation of Fe-carbonate.

A graphite-rich carbonate vein, located in the northeastern part of the ISB, contains high concentrations of graphite (sample 4062002y, 4.1 wt% C; see Supplementary Table 3) compared with other carbonate veins in the ISB, which contain much smaller amounts of graphite if any (see Supplementary Information). Such secondary graphite was analysed together with graphite in the metasediment. The geothermometric signals of the Raman spectrum in metasediment sample 6072905 indicate that peak metamorphic temperatures of the graphite were $525 \pm 50\,°C$, which is consistent with prograde metamorphic temperatures reported for the ISB (500–600 °C; ref. 9). This temperature consistency

[1]Natural Resources and Environmental Geochemistry Research Group, Division of Earth and Planetary Materials Science, Graduate School of Science, Tohoku University, 980-8578, Japan, [2]Nordic Center for Earth Evolution, Natural History Museum of Denmark, University of Copenhagen, 1350, Denmark.
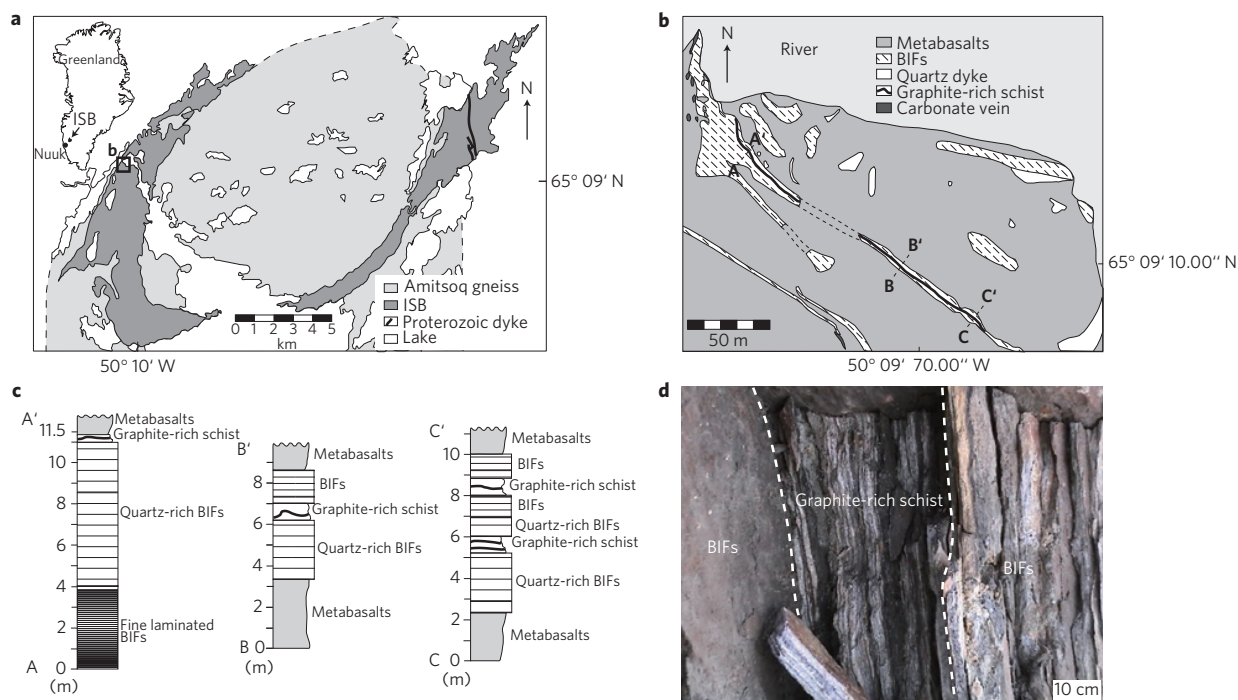*e-mail: ohtomoy@jamstec.go.jp

25

**Figure 1 | Geologic maps and photos of the study area in the ISB, West Greenland. a**, General geology of the ISB, West Greenland. **b**, Geologic map produced in this study. **c**, Geologic cross-sections A–A′ (northern section), B–B′ (central section) and C–C′ (southern section). Points along A–C′ are the same as those presented in **b**. **d**, Outcrop photograph of graphite-rich schist intercalated with BIFs.
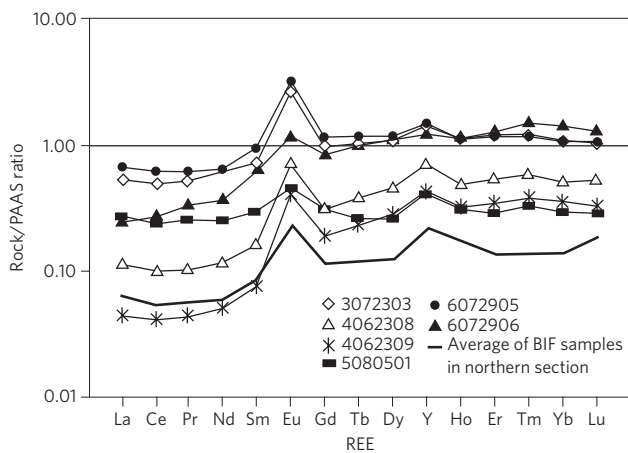


**Figure 2 | REE patterns in the examined graphite-rich schist.** The BIF value in this figure represents the average composition of nine BIF samples from along the northern section A–A′ (Fig. 1b).

suggests that the precursor of the graphite was already present in the host rocks before prograde metamorphism. Raman spectrum of secondary graphite (sample 4062002y) is nearly identical to that of the graphite in the metasediment. The estimated metamorphic temperatures for the secondary graphite ($496 \pm 50\,°C$) are close to peak metamorphic temperatures, suggesting a metamorphic origin of the secondary graphite.

The carbon isotope ratios ($\delta^{13}C$) of graphite were determined using the graphite combustion method and the neodymium–yttrium aluminium garnet (Nd–YAG) laser microprobe technique. The range of $\delta^{13}C$ values was $-23.8$ to $-12.5‰$ (average, $-17.9‰$), which is within the range of values reported in previous studies (Fig. 3). The $\delta^{13}C$ value of the secondary graphite (sample 4062002y) was $-10.5‰$ (Supplementary Table 3). The Nd–YAG laser microprobe analysis revealed microscale heterogeneities

in the $\delta^{13}C$ values in single rock chips ($10 \times 5 \times 0.5\,mm^3$; Fig. 3b,c and Supplementary Fig. 2). For example, the $\delta^{13}C$ values for sample 5080603 ranged from $-20.9$ to $-14.7‰$ (average, $-17.4‰$; Fig. 3c).

Carbonic fluids can precipitate abiogenic graphite during isobaric cooling, during isothermal increases in pressure[12] and on account of the mixing of $CH_4$- and $CO_2$-rich fluids[13]. We modelled the theoretical $\delta^{13}C$ values of fluid-precipitated graphites[14], assuming that the $\delta^{13}C$ value for $CO_2$ in the original metamorphic fluid was $-5‰$, which is similar to the value observed regionally in carbonate-rich rocks of the ISB (refs 4,7). The lightest $\delta^{13}C$ value for graphite precipitated from such fluids under metamorphic conditions is $-16.4‰$, which is achieved at $400\,°C$ (Supplementary Fig. 5a). The $\delta^{13}C$ values exceed $-16.4‰$ when Rayleigh-type isotope fractionation operates in the fluids. Graphite that is depleted in $^{13}C$ by more than $-16.4‰$ can form only if the fluid was derived from a source that already contained abundant $^{13}C$-depleted $CH_4$. However, given the possible oxidation state of infiltrating metamorphic fluids, $CH_4$ was most probably absent in the fluids (see Supplementary Information).

In samples from central to southern sections (B–B′ and C–C′, respectively; Fig. 1), abundances of $C_{graphite}$ were low and $\delta^{13}C$ values were high, suggesting that extensive reactions with metamorphic fluids shifted $\delta^{13}C$ of graphite to higher $\delta^{13}C$ values (for example, $-12.5‰$; Supplementary Fig. 3). The heterogeneities in $\delta^{13}C$ values (Fig. 3a–c) are explained by exchange of carbon isotopes with transient carbonic fluids. In other words, all $\delta^{13}C$ of graphite were originally lower than those shown in Fig. 3. The more negative isotopic compositions (for example, $-23.8‰$) represent less modified components and are closer to premetamorphic compositions. Therefore, $^{13}C$-depleted organic matter in Isua clastic sediments is postulated as an initial carbon source to explain the less modified carbon isotope compositions.

We observed the morphologies and nanostructures of graphite in the metasediment and secondary graphite using scanning transmission electron microscopy (STEM) and high-resolution
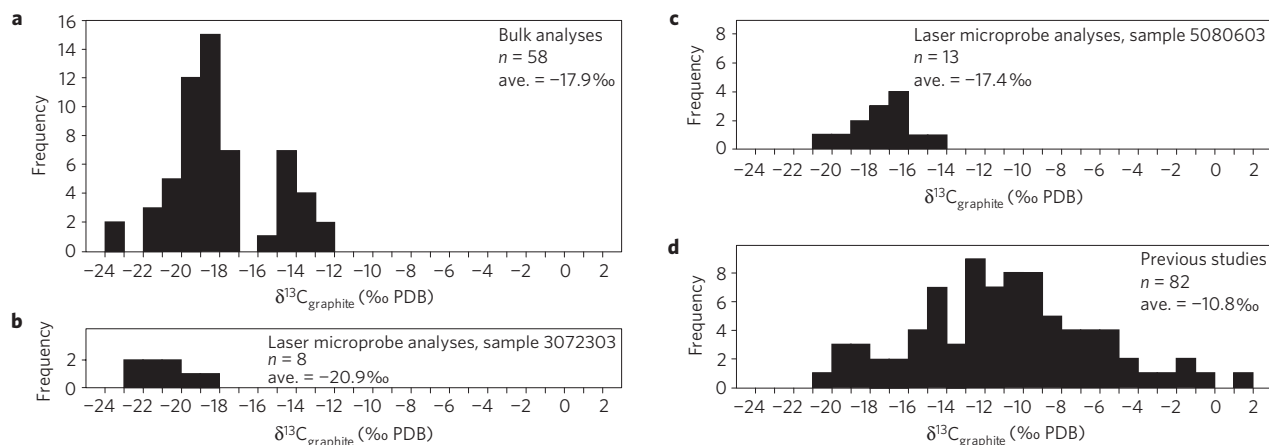
**Figure 3 | Carbon stable isotope compositions of graphite in the ISB. a**, $\delta^{13}$C values for graphite in graphite-rich schist extracted from bulk rock powder. **b**, $\delta^{13}$C values for graphite in sample 3072303 obtained using the Nd–YAG laser microprobe technique. **c**, $\delta^{13}$C values for graphite in sample 5080603 obtained using the Nd–YAG laser microprobe technique. **d**, Total range of published $\delta^{13}$C values for graphite in the ISB. Referenced data are listed in Supplementary Table 6. *n*, number of analyses; ave., average value; PDB, Pee Dee Belemnite. Reproducibilities and accuracies of measurements are within ±0.2‰.
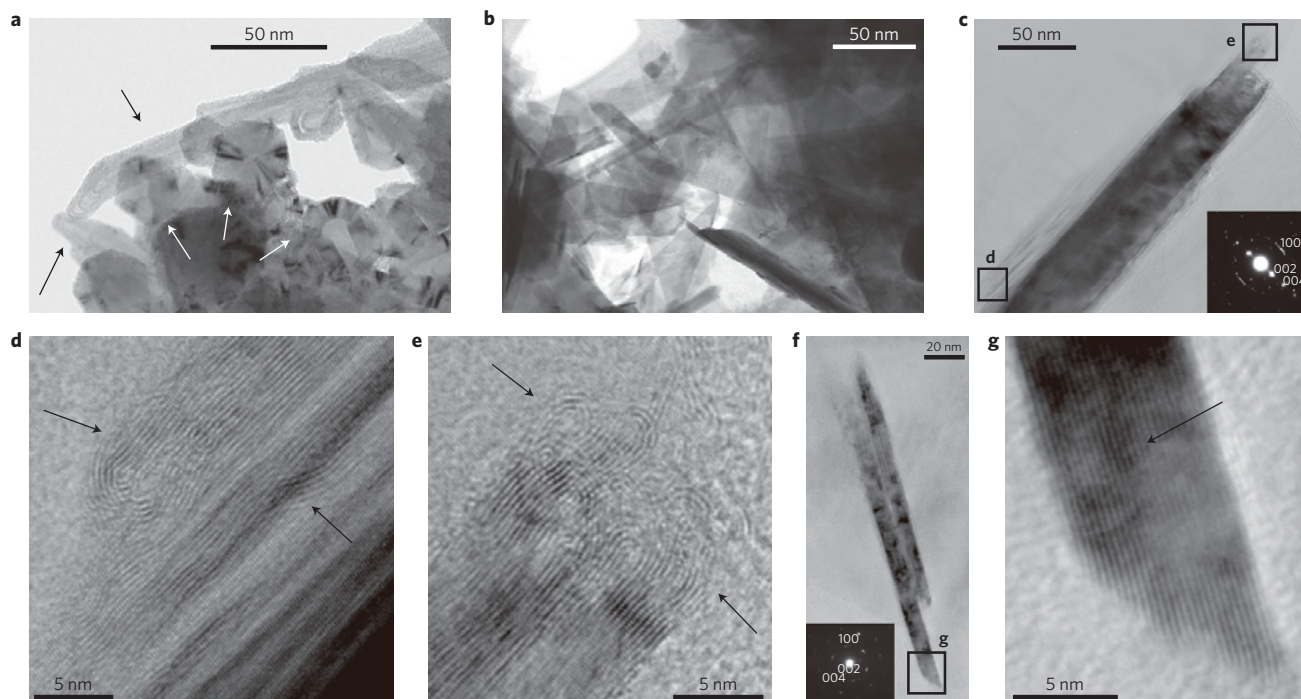


**Figure 4 | Transmission electron microscopy images of graphite. a**, STEM image of graphite in metasediment (sample 6072906), showing dominance of polygonal and tube-like grains. **b**, STEM image of secondary graphite (sample 4062002y), showing dominance of sheeted flake grains. **c**, HRTEM image of graphite in metasediment (sample 6072905). SAED was obtained from area in **c**. **d,e**, Magnification of the area marked **d** and **e** in **c**. **f**, HRTEM image of sample 4062002y. SAED was obtained from area in **f**. **g**, Magnification of the area marked **g** in **f**. Arrows are explained in the main text.

transmission electron microscopy (HRTEM). Irrespective of the sample type, all examined graphite showed highly crystalline features in HRTEM observations, which is consistent with the XRD and Raman data. Differences between graphite in the metasediment and that in the secondary vein samples are reflected in their respective morphologies, internal graphite nanostructures and stacking defects. The examined metasediment included graphitic polygonal grains (white arrows, Fig. 4a) and tube-like structure (black arrows, Fig. 4a). Some lattice fringes showed distortion at surfaces and inside graphite grains (onion-like structures; black arrows, Fig. 4d,e; see Supplementary Information for details). Such features were found in samples from both

the northern and southern sections (Supplementary Fig. 9a,b). Sheeted flakes were a dominant morphology of secondary graphite, whereas polygonal grains and tube-like structures were absent (Fig. 4b). The sheeted flakes indicate well-layered structures overall (Fig. 4f,g), although the surfaces and edges of flakes were sometimes curled. Such curled structures disappear on the inner portions of sheeted flakes (black arrow, Fig. 4g; white arrows, Supplementary Fig. 8d,e). The structural changes from the surface to the inner portions of the sheeted flakes indicate that initial deposition of distorted graphite (on the current surface) was followed by ordered deposition of successive layers of graphite (current inner part)[15].

In contrast, curled structures are present in the inner portions of graphite grains in the metasediment (black arrows, Fig. 4d), suggesting that its origin is different from that of the secondary graphite. The selected area electron diffraction (SAED) pattern of graphite in the metasediment has $\langle 001\rangle^*$ streaks on and near the $h00$ reflections (see the bright diffusion line near the 100 plane in the SAED data, Fig. 4c), caused by a disordered stacking sequence of the graphene sheets. However, $\langle 001\rangle^*$ streaks are unclear in the SAED pattern of Fig. 4f, suggesting a dominance of ordered 2H-type stacking in the secondary graphite.

The effects of temperature, pressure and mineral surfaces on the graphitization of biogenic organic compounds in geological samples have been intensively studied[16–22]. Distorted structures and the diffusion of graphene sheet stacking are common in pyrolysed and pressurized organic compounds. Such precursors commonly contain non-graphitizing carbon, such as non-planar carbon ring compounds associated with abundant pores[16]. At high pressures, organic matter in the presence of various hydrocarbons mixed with non-graphitizing carbon is forced into parallelism, thereby facilitating the formation of hexagonal graphene sheets, whereas the crystal lattice remains distorted and the graphene sheet stacking may display diffusion in SAED patterns. Therefore, biogenic organic matter, which contains various molecules and functional groups, is favoured as the precursor of the graphite observed in the metasediment.

Onion-like carbonaceous materials have also been observed in meteorites[23]. Some onion-like carbonaceous materials in meteorites were formed at >1,000 °C (ref. 23), which exceeds general metamorphic temperatures. Furthermore, graphite in the examined schist has sedimentary characteristics with various morphologies, suggesting that meteoritic origin is unlikely for the Isua graphite. Polygonal and tube-like structures in graphite-rich schist show similarities to those found in artificial nanocarbons formed under evaporation–condensation conditions and in electric discharge systems[15,24]. However, unusual temperature conditions and chemistry of carbon sources to generate artificial nanocarbons are difficult to realize in the Earth's crust. Therefore, we conclude that polygonal and tube-like structures in the graphite-rich schist were generated during maturation processes of organic matter. A minor portion of heterogeneity in the graphitic structural order could be caused by the secondary effects of surrounding minerals[22] and/or dynamic fluid flow processes[15] during metamorphism.

Graphite in the metasediment from the northwest ISB is distinct from the graphite in vein samples. The combined information on geological occurrences, graphite morphologies, nanoscale structures and isotopic compositions of the graphite in the metasediment suggests a biogenic origin. High concentrations of $^{13}$C-depleted graphite in these rocks would require widespread biological activity to support the high rate of production and sedimentary delivery of organic matter to the >3.7 Ga ocean floor.

## References

1. Nutman, A. P., Friend, C. R. L. & Paxton, S. Detrital zircon sedimentary provenance ages for the Eoarchaean Isua supracrustal belt southern West Greenland: Juxtaposition of an imbricated ca. 3700 Ma juvenile arc against an older complex with 3920–3760 Ma components. *Precambrian Res.* **172**, 212–233 (2009).
2. Rosing, M. T. $^{13}$C-depleted carbon microparticles in >3700-Ma sea-floor sedimentary rocks from west Greenland. *Science* **283**, 674–676 (1999).
3. Naraoka, H., Ohtake, M., Maruyama, S. & Ohmoto, H. Non-biogenic graphite in 3.8-Ga metamorphic rocks from the Isua district, Greenland. *Chem. Geol.* **133**, 251–260 (1996).
4. Van Zuilen, M., Lepland, A. & Arrhenius, G. Reassessing the evidence for the earliest traces of life. *Nature* **418**, 627–630 (2002).
5. Mojzsis, S. J. *et al.* Evidence for life on Earth before 3,800 million years ago. *Nature* **384**, 55–59 (1996).
6. Fedo, C. M. & Whitehouse, M. J. Metasomatic origin of quartz–pyroxene rock, Akilia, Greenland, and implications for Earth's earliest life. *Science* **296**, 1448–1452 (2002).
7. Schidlowski, M., Appel, P. W. U., Eichmann, R. & Junge, C. E. Carbon isotope geochemistry of the $3.7 \times 10^9$-yr-old Isua sediments, West Greenland: Implications for the Archaean carbon and oxygen cycles. *Geochim. Cosmochim. Acta* **43**, 189–199 (1979).
8. Ueno, Y., Yurimoto, H., Yoshioka, H., Komiya, T. & Maruyama, S. Ion microprobe analysis of graphite from ca. 3.8 Ga metasediments, Isua supracrustal belt, West Greenland: Relationship between metamorphism and carbon isotopic composition. *Geochim. Cosmochim. Acta* **66**, 1257–1268 (2002).
9. Rose, N. M., Rosing, M. T. & Bridgwater, D. The origin of metacarbonate rocks in the Archaean Isua supracrustal belt, West Greenland. *Am. J. Sci.* **96**, 1004–1044 (1996).
10. Rosing, M. T., Rose, N. M., Bridgwater, D. & Thomsen, H. S. Earliest part of Earth's stratigraphic record: A reappraisal of the >3.7 Ga Isua (Greenland) supracrustal sequence. *Geology* **24**, 43–46 (1996).
11. Taylor, S. R. & McLennan, S. M. *The Continental Crust: Its Composition and Evolution* (Blackwell, 1985).
12. Luque, F. J. & Rodas, M. Constraints on graphite crystallinity in some Spanish fluid-deposited occurrences from different geologic settings. *Miner. Deposita* **34**, 215–219 (1999).
13. Chamberlain, C. P. & Rumble, D. Thermal anomalies in a regional metamorphic terrane: An isotopic study of the role of fluids. *J. Petrol.* **29**, 1215–1232 (1988).
14. Ray, J. S. Carbon isotopic variations in fluid-deposited graphite: Evidence for multicomponent Rayleigh isotopic fractionation. *Int. Geol. Rev.* **51**, 45–57 (2009).
15. Kuznetsov, V. L., Butenko, Y. V., Zaikovskii, V. I. & Chuvilin, A. L. Carbon redistribution processes in nanocarbons. *Carbon* **42**, 1057–1061 (2004).
16. Buseck, P. R. & Bo-Jun, H. Conversion of carbonaceous material to graphite during metamorphism. *Geochim. Cosmochim. Acta* **49**, 2003–2016 (1985).
17. Large, D. J., Christy, A. G. & Fallick, A. E. Poorly crystalline carbonaceous matter in high-grade metasediments—implications for graphitization and metamorphic fluid compositions. *Contrib. Mineral. Petrol.* **116**, 108–116 (1994).
18. Deurbergue, A., Oberlin, A., Oh, J. H. & Rouzaud, J. N. Graphitization of Korean anthracites as studied by transmission electron microscopy and X-ray diffraction. *Int. J. Coal Geol.* **8**, 375–393 (1987).
19. Rouzaud, J. N. & Oberlin, A. Structure, microtexture, and optical properties of anthracene and saccharose-based carbons. *Carbon* **27**, 517–529 (1989).
20. Bustin, R. M., Ross, J. V. & Rouzaud, J. N. Mechanisms of graphite formation from kerogen: Experimental evidence. *Int. J. Coal Geol.* **28**, 1–36 (1995).
21. Beyssac, O. *et al.* Graphitization in a high-pressure, low-temperature metamorphic gradient: A Raman microspectroscopy and HRTEM study. *Contrib. Mineral. Petrol.* **143**, 19–31 (2002).
22. Van Zuilen, M. A. *et al.* Mineral-templated growth of natural graphite films. *Geochim. Cosmochim. Acta* **83**, 252–262 (2012).
23. Le Guillou, C. *et al.* High resolution TEM of chondritic carbonaceous matter: Metamorphic evolution and heterogeneity. *Meteorit. Planet. Sci.* **47**, 345–362 (2012).
24. Horváth, Z. E. *et al.* Inexpensive, upscalable nanotube growth methods. *Curr. Appl. Phys.* **6**, 135–140 (2006).

## Author contributions

Y.O., T.K. and M.T.R. conducted the geological surveys and collected rock samples. Y.O. carried out the geological and petrographical analyses, carbon stable isotope analyses of graphite using the graphite combustion method, XRD analyses, HRTEM observations and thermodynamic/isotopic calculations. A.I. and T.N. contributed to sample preparation and HRTEM observations. T.K. carried out carbon stable isotope analyses of graphite using the *in situ* Nd–YAG laser microprobe technique, STEM observations and Raman microspectroscopic analyses.

## Additional information

Supplementary information is available in the online version of the paper. Reprints and permissions information is available online at www.nature.com/reprints. Correspondence and requests for materials should be addressed to Y.O.

## Competing financial interests

The authors declare no competing financial interests.

# Evidence for biogenic graphite in early Archaean Isua metasedimentary rocks

Yoko Ohtomo[1], Takeshi Kakegawa[1], Akizumi Ishida[1], Toshiro Nagase[1] and Minik T. Rosing[2]

[1]Natural Resources and Environmental Geochemistry Research Group, Division of Earth and Planetary Materials Science, Graduate School of Science, Tohoku University, Japan [2]Nordic Center for Earth Evolution, Natural History Museum of Denmark, University of Copenhagen, Denmark

**Supplementary data**

*Geology*

The Isua Supracrustal Belt (ISB) is part of the ~3.8-billion-year-old sedimentary Itsaq Gneiss Complex of Southwest Greenland. These rocks have experienced amphibole-facies prograde metamorphism (~500–600°C, ~5 kbar). The western section of the ISB is mainly composed of two major packages of volcanic and volcanogenic sedimentary rocks: (1) the "Garbenschiefer Unit", which consists of a succession of basaltic lavas, interstratified volcanogenic sedimentary horizons, and interbedded BIFs, which is bounded by (2) the "Amphibolite Unit" and metagabbros[10].

The study area, located in the Garbenschiefer Unit, is approximately 1 km north of the Bouma sequence[2]. The key rocks in the study area are BIFs with vertical dips and strikes ranging from N40E to N45E. In general, five horizons of BIFs are found in the area (Fig. 1). Graphite-rich schist occurs in the thickest BIF in the study area. Geologic columns were constructed for the regions of the northern A–A′ section, the central B–B′ section, and the southern C–C′ section (Fig. 1c). Graphite-rich schist occurs within the BIFs in the central and northern sections. In the southern section, two layers of graphite-rich schist were identified in the same BIF.

*Petrography*

The mineral assemblages of the graphite-rich schist are summarized in Supplementary Table S1. Photomicrographs of thin sections and back-scatter electron images of typical samples are shown in Supplementary Figure S1.

Northern section samples

All samples in the northern section show fine banding at microscopic scales, which is interpreted as remnants of sedimentary bedding.

Samples 3072303 and 6072905. These samples contain abundant $^{13}C$-depleted graphite (Supplementary Table S3) and are rich in chlorite, cummingtonite–anthophyllite, and quartz (Supplementary Table S1 and Supplementary Fig. S1a, f, g and h). Fine-grained chlorite, together with graphite, is aligned parallel to fine laminations, whose orientation is the same as that of surrounding BIF layering. Cummingtonite and anthophyllite grains, observed in quartz-rich layers, are up to 100 μm in diameter. Minor minerals are also present in both samples, including zircon (anhedral to subhedral, 2 μm in diameter), apatite, monazite, and ilmenite (30 μm in diameter).

Samples 4062306, 4062307, 4062308, and 4062309. These samples are rich in euhedral to subhedral cummingtonite (50–150 μm in diameter) and anhedral quartz (10–50 μm in diameter). Laminations are developed at the millimetre-scale and graphite is found within specific laminations. Chlorite is a minor component.

Samples 5080501, 5080502, 5080503, and 6072906. These samples are rich in cummingtonite (diameters up to 100 μm), which is associated with abundant graphite and quartz. Unlike the other samples in the northern section, no separate quartz-rich laminations are apparent.

Central section samples

Sample 4062611. This sample, which is dominated by quartz, cummingtonite, and chlorite, lacks fine laminations at the scale of individual thin sections because of intense metamorphism. The matrix is dominated by fine-grained chlorite (~10 μm in diameter).

Southern section samples

Samples 4062710, 5080401, and 5080402. These samples are mainly dominated by fine-grained chlorite (~10 μm in diameter) and include quartz and cummingtonite. No fine laminations are visible in thin sections. Quartz veinlets (several millimetres in width) cut across chlorite–graphite-rich sections.

Samples 4062709 and 5080603. These samples, which are rich in ilmenite, chlorite, cummingtonite, and quartz, contain coarse laminations. The samples consist of quartz–cummingtonite-rich layers and chlorite–graphite–anthophyllite-rich layers. The thicknesses of each layer range from several hundred micrometers to a few millimetres. Most of the cummingtonite is euhedral and about 30 μm in diameter. Graphite occurs in the chlorite-rich parts.

Graphite-rich carbonate veins

Sample 4062002y was collected from a graphite-rich carbonate vein at the same location as that of sample AL7-2 of Van Zuilen et al. (2002)[4], on the northeastern side of the ISB. This sample is a massive metacarbonate, composed mainly of siderite, magnetite, amphibole, and graphite, which is unlike the composition of the graphite-rich schist in terms of the presence of siderite and magnetite. Metacarbonate, which evolved within the amphibole–chlorite–garnet schists, is interpreted as metamorphosed ocean basalt, which clearly indicates its secondary origin. The concentration of $\delta^{13}C_{graphite}$ in the sample is −10.5‰.

***Chemical compositions***

The chemical compositions of typical samples are listed in Supplementary Table S2. Carbon concentrations and $\delta^{13}$C values (bulk analyses) for all samples are listed in Supplementary Table S3.

Northern section samples

Samples 3072303 and 6072905. The chemical compositions of these two samples are similar. Sample 3072303 contains 67.44 wt% $SiO_2$, 13.70 wt% $Fe_2O_3$, 4.98 wt% $Al_2O_3$, and 0.22 wt% $TiO_2$, and contains high concentrations of V (39.07 ppm), Zr (51.61 ppm), Th (1.95 ppm), U (0.47 ppm), and Cr (115.04 ppm); the Cr concentration in sample 3072303 is the highest of all samples analysed in the study. Sample 6072905 also contains high concentrations of $Al_2O_3$ (6.24 wt%), V (49.00 ppm), Cr (80.00 ppm), Zr (75.00 ppm), Th (3.20 ppm), and U (0.60 ppm). Observations using a scanning electron microscope-energy dispersive spectroscopy indicate that the Ti occurs mainly in ilmenite.

Samples 4062306, 4062307, 4062308, and 4062309. The $SiO_2$ contents in these samples are relatively high, ranging from 73.92 to 81.45 wt%. The $Fe_2O_3$ contents range from 12.81 to 17.68 wt%, and the $Al_2O_3$ contents, which range from 0.05 to 0.11 wt%, correspond to low $TiO_2$ contents (0.01 wt%). The samples contain moderate amounts of Zr (3.94–6.39 ppm), Th (0.10–0.22 ppm), and U (0.05–0.1 ppm). The V and Cr contents are below the limits of detection.

Samples 5080501, 5080502, 5080503, and 6072906. The $SiO_2$ and $Fe_2O_3$ contents in these samples range from 52.44 to 62.56 wt% and from 26.95 to 37.03 wt%, respectively. The $Al_2O_3$ contents are low (0.09–0.43 wt%), corresponding to low $TiO_2$ concentrations (0.01–0.03 wt%). The Cr contents are moderate (20.00–40.00 ppm).

Central section samples

Sample 4062611. This sample contains 0.4 wt% graphite. The $SiO_2$ and $Fe_2O_3$ contents are 57.88 wt% and 14.64 wt%, respectively. The $Al_2O_3$ content is low (0.49 wt%), as is the $TiO_2$ content (0.01 wt%). The MgO content is extremely high (23.32 wt%), and the sample also contains moderate amounts of Zr (7.06 ppm), Th (0.08 ppm), and U (0.06 ppm). The V and Cr contents are below the limits of detection.

Southern section samples

Samples 4062710, 5080401, and 5080402. These samples contain 0.2–0.4 wt% graphite, 60.78–81.55 wt% $SiO_2$, and 10.03–12.37 wt% $Fe_2O_3$. The $Al_2O_3$ contents are low (0.14–0.42 wt%), as are the $TiO_2$ contents (<0.03 wt%).

Sample 4062709. This sample contains 0.5 wt% graphite, 75.11 wt% $SiO_2$, and 15.61 wt% $Fe_2O_3$; the $Al_2O_3$ content is low (0.30 wt%), as is the $TiO_2$ content (<0.01 wt%). The sample contains moderate amounts of Cr (40.00 ppm) and Th (0.20 ppm), but contents of V, Zr, Th, and U are all below the limits of detection.

### *Raman microspectroscopy*

The Raman spectrum of well-ordered graphite consists of several bands. The first-order band, located at ~1582 $cm^{-1}$ (designated as the G band), is attributed to C–C vibrations of aromatic carbon. Disordered carbonaceous matter usually displays additional first-order bands (designated as D bands) located at ~1355 $cm^{-1}$ (D1 band), ~1550 $cm^{-1}$ (D3 band), and ~1620 $cm^{-1}$ (D2 band), and a second-order band at ~2900 $cm^{-1}$. In this study, we focused on the 1050–1850 $cm^{-1}$ region, which includes all first-order bands. Examples of Raman spectra, obtained from samples 4062002y and 6072905, are presented in Supplementary Figure S4. The G and D1 bands of sample 4062002y are located at approximately 1581 and 1354 $cm^{-1}$, respectively. The G and D1 bands of sample 6072905 are located at approximately 1584 $cm^{-1}$ and 1358 $cm^{-1}$, respectively. The results of spectral decomposition for all spots, the position and FWHM of the G bands, the D1/G peak intensity ratios (R1) (i.e., peak heights), and the D1/(G+D1+D2) peak area ratios (R2) are summarized in Supplementary Table S5. The progressive graphitization of carbonaceous grains with increasing temperature, which forms the basis of the metamorphic thermometer for metasedimentary rocks, can be expressed as follows[25]:

$$T \ (°C) = -455 \times R2 + 641 \pm 50$$

### *Heterogeneity of $\delta^{13}C_{graphite}$ and graphite concentrations*

The $\delta^{13}C_{graphite}$ values of the examined metasediment show regional variations that correlate with petrographic features and graphite concentrations. The $\delta^{13}C_{graphite}$ values are heterogeneous, even in bulk analyses of the same sample, suggesting that $\delta^{13}C_{graphite}$ heterogeneities are localized in small areas. The $\delta^{13}C_{graphite}$ values for samples from the northern section (A–A′, Fig. 1) are more $^{13}C$-depleted than for samples from the central section (B–B′) and the southern section (C–C′) (Supplementary Fig. S3a); graphite concentrations are also highest in samples from the northern section. Irregular silicification, which appears in schist samples with relatively high silica concentrations, reduces graphite concentrations. It is likely that the heterogeneities in the $\delta^{13}C_{graphite}$ values in samples from the northern and southern sections are caused by carbon isotope exchange between graphite-rich schist and carbonic fluids (Supplementary Fig. S3b).

### *Calculation of $\delta^{13}C$ values for graphite precipitated from metamorphic fluids*

The carbon isotope compositions of $CO_2$ and $CH_4$ in metamorphic fluids are modified by the precipitation of abiogenic graphite. Rayleigh isotopic fractionation describes the systematic changes in carbon isotope compositions in such a system. We calculated the $\delta^{13}C_{graphite}$ values of fluid-precipitated graphite using single-component ($CO_2$) and multi-component ($CH_4$ and $CO_2$) Rayleigh isotopic fractionation models at the metamorphic temperatures 400°C, 500°C, and 600°C by reference to Ray (2009)[14]. The single-component model is expressed by the following reaction:

$$\delta^{13}C_{graphite} = \alpha_{g-1}(\delta^{13}C_{initial\ source} + 1000)F^{\alpha-1} - 1000.$$

Calculations of the multi-component model were performed as follows:

$$\delta^{13}C_{graphite} = \{\alpha_{g-1}/(a - b/F) - 1\} + \{\alpha_{g-1}/(a - b/F)\}\ \delta^{13}C_{source} \times 10^3$$

where

$$a = (1 + \alpha_{CH4-CO2})/2$$
$$b = (1 - r_{CH4-CO2})(\alpha_{CH4-CO2} - 1)/2(1 + r_{CH4-CO2})$$

and

$$\delta^{13}C_{source} - \delta^{13}C_{initial\ source} \approx [\alpha_{g-1}\ \{\ln(aF - b)/(a - b)\}/a - \ln F] \times 10^3$$

In these equations, $\alpha_{g-1}$ is the fractionation factor of carbon between graphite and the largest source component (in this case, $CO_2$ gas), F is the fraction of remaining carbon in the source, $\alpha_{CH4-CO2}$ is the fractionation factor of carbon between $CH_4$ and $CO_2$, and $r_{CH4-CO2}$ is the ratio of the initial number of moles of a component to the first component ($CH_4$ and $CO_2$). The compounds $CH_4$ and $CO_2$ were assumed to be in constant isotopic equilibrium at the given temperature. In the system, initial $\delta^{13}C_{CH4}$ values were –24.2‰, –20.2‰, and –17.7‰ at 400°C, 500°C, and 600°C, respectively[26]. The $\delta^{13}C$ value of $CO_2$ in the original metamorphic fluid was assumed to be –5‰, which is consistent with actual $\delta^{13}C$ values of carbonates in the ISB. The results, summarized in Supplementary Figure S5, show that the lightest possible value of –16.4‰ occurs in a single-component model (Supplementary Fig. S5a).

If the dominant carbon-bearing species in the metamorphic fluid is $^{13}C$-depleted $CH_4$, the production of $^{13}C$-depleted graphite might occur by the *in situ* oxidation of $CH_4$ or by a Fischer-Tropsch-type synthesis. We estimated the compositions of carbonic fluids, assuming filtration of fluids by the BIFs surrounding the graphite-rich schist[27–29]. During metamorphism, the stability fields of $CO_2$ and $CH_4$ can be constrained by the following reaction, the equilibrium constant K, the fugacity f, and the temperature T[27]:
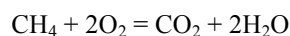
$$CH_4 + 2O_2 = CO_2 + 2H_2O$$
$$K = f_{CO2}(f_{H2O})^2/f_{CH4}(f_{O2})^2$$
$$\log K = 41997/T + 0.719\log T - 2.404$$

We assumed that $f_{H2O} = 1$ and $f_{CH4} = (1 - \beta)f_{CO2}$, and calculated $f_{O2}$ in terms of a series of $\beta$ values ($\beta = 0$, 0.4, 0.7, 0.8 and 0.9) at pressures of 2 and 5 kbar (Supplementary Fig. S6a and b). We also estimated $f_{O2}$ from logK, as calculated by SPUCRT92, for comparison (Supplementary Fig. S6c and d). These results indicate that the carbonic fluids buffered by grunerite/cummingtonite–magnetite BIFs were dominated by $CO_2$; $f_{CH4}/f_{CO2} \leq 0.3$ ($\beta \geq 0.7$) (Supplementary Fig. S6d). Therefore, if the fluids infiltrate the cummingtonite/grunerite–magnetite BIFs around the graphite-rich schist, the majority of $CH_4$ in metamorphic fluids is probably converted to $CO_2$, as cummingtonite/grunerite and magnetite control the oxidation state of fluids in Ni–NiO (NNO) buffering conditions, stabilizing $CO_2$ rather than $CH_4$ under the pressure–temperature conditions of the amphibolite metamorphic facies. Given all these factors, it is unlikely that abundant abiogenic graphite could have been precipitated in the examined metasediment.

### TEM images

Figure 4 of the main text and Supplementary Figures S7–S9 show scanning transmission electron microscope (STEM), high-resolution transmission electron microscope (HRTEM), and selected area electron diffraction (SAED) images. We examined the SAED data to constrain the d spacing and stacking fault. In addition, we cross-referenced transmission electron microscope (TEM) data with Raman microspectroscopic and X-ray diffratcion data. However, all samples, including sedimentary and secondary vein graphite samples, show nearly identical results, because all graphite has experienced the same degree of metamorphism. On the other hand, differences are apparent in the morphologies and nanostructures, and in some of the SAED data. Characteristics of each figure are explained in the main text and in the figure captions. The morphologies of graphite grains, as observed in STEM images, differ between the metasediment and secondary veins. Minor curled structures are present in secondary vein samples, but such structures are likely to disappear during grain growth. Some distorted and curled structures are common in graphite from metasediment in both of the northern and southern sections.
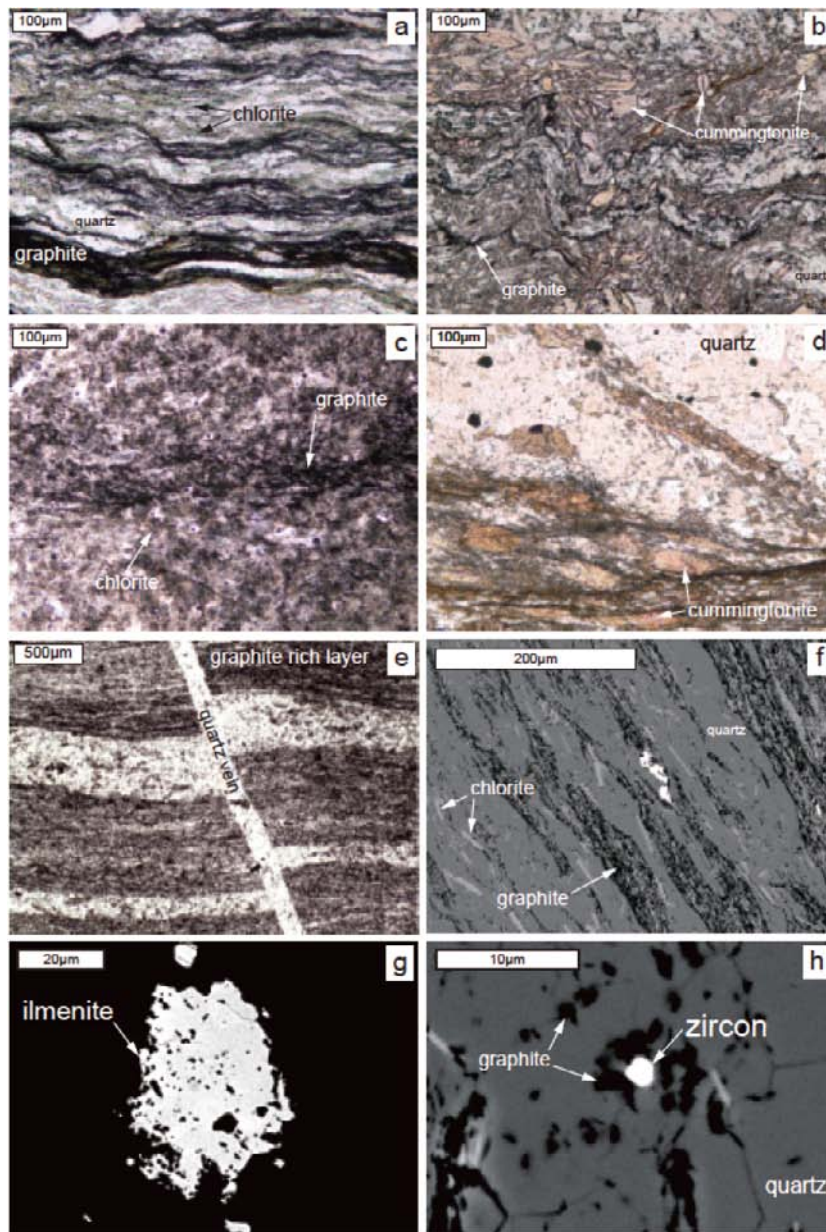
**Figure S1 | Photomicrographs of thin sections and back-scatter electron images of typical samples.**
**a**, Sample 3072303, which comprises graphite, chlorite, and quartz, contains fine laminations. **b**, Cummingtonite, graphite, and quartz are the dominant minerals in sample 4062308. **c**, No laminations are visible in sample 4062611. **d**, Cummingtonite and quartz are observed mainly in sample 4062710. **e**, Sample 5080603 exhibits distinct graphite-rich and quartz-rich laminations. **f**, Graphite coexists with chlorite in sample 6072905. **g**, Ilmenite is present in sample 6072905. **h**, Zircon in sample 6072905.
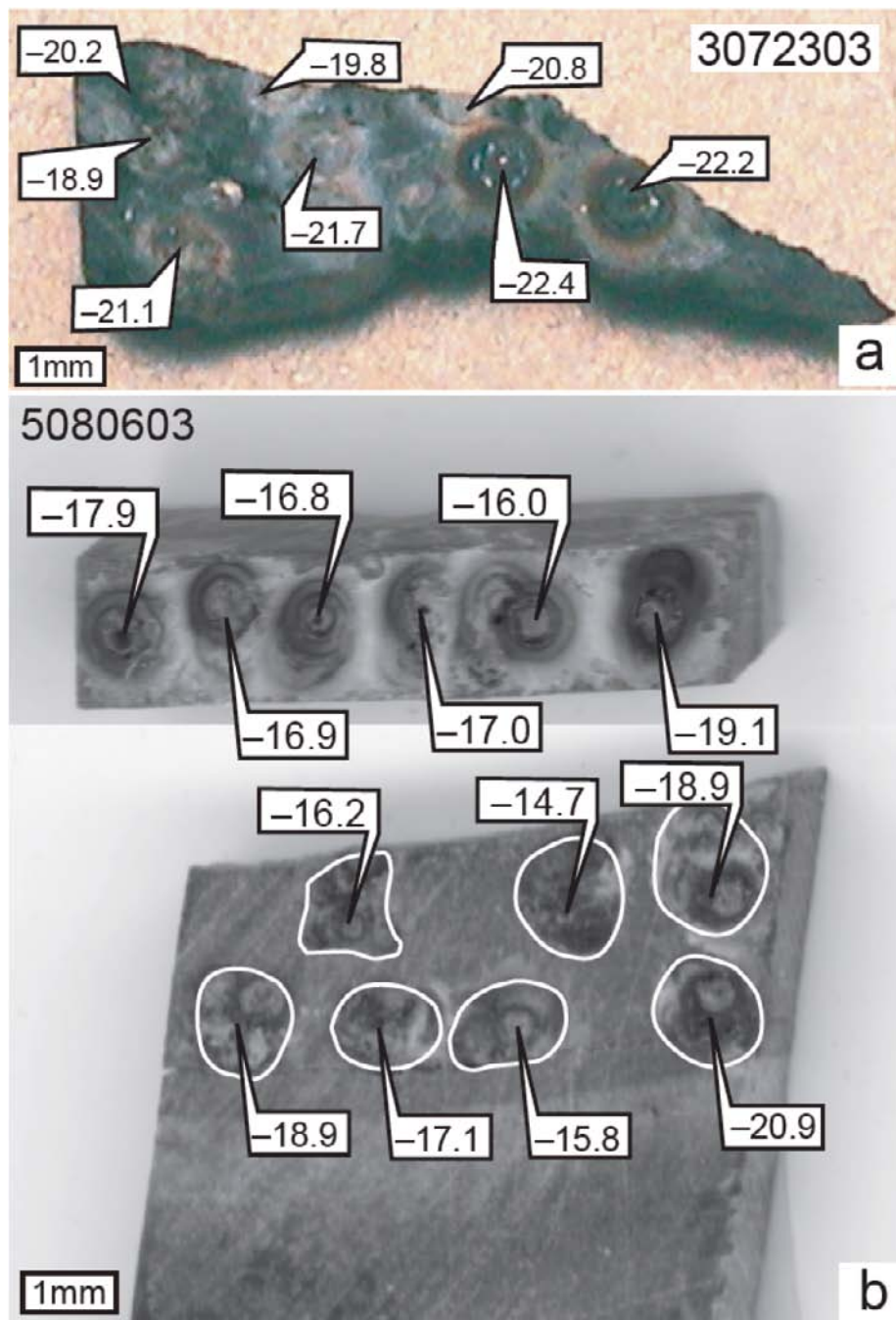
**Figure S2 | Photographs of examined rock fragments and carbon stable isotope values determined by the Nd–YAG laser microscopic technique**. **a**, Sample 3072303 from the northern section of the graphite-rich schist. **b**, Sample 5080603 from the southern section of the graphite-rich schist. The numbers in each figure represent carbon isotope compositions. In the lower image, laser ablation was performed on a vertical section, which contains two graphite-rich layers. Because of low concentrations of graphite in the vertical sections, laser ablations were performed at 2 or 3 locations, as indicated by white circles.
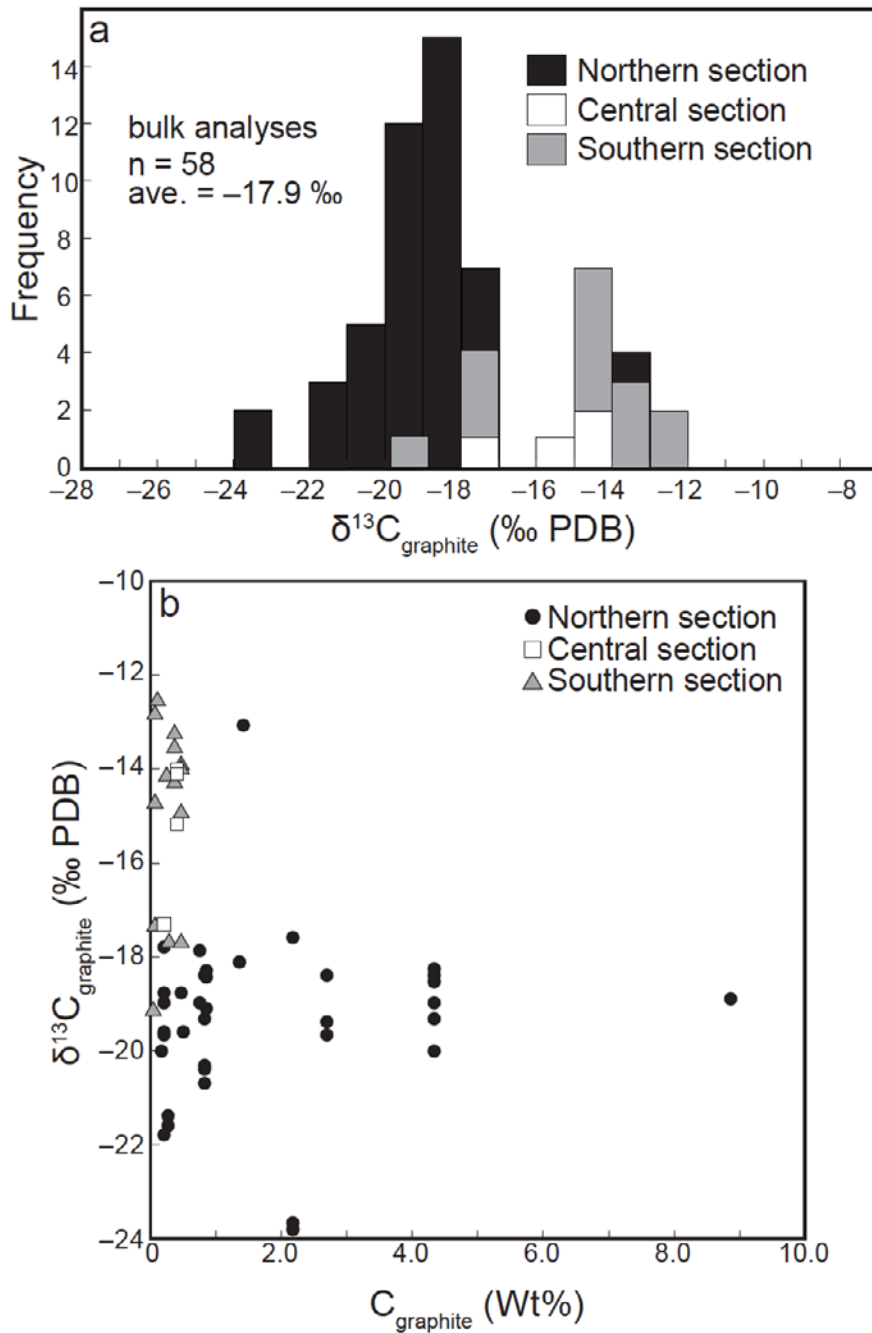
**Figure S3 | δ$^{13}$C values of graphite extracted from bulk rock powders and correlation between graphite concentrations and δ$^{13}$C values of graphite**. **a**, $^{13}$C-depleted carbon isotope values are predominant in graphite from northern section compared to central and southern sections. **b**, Samples from northern section reveal high graphite concentration and low δ$^{13}$C values of graphite, whereas Samples from central and southern sections reveal low graphite concentration and high δ$^{13}$C values of graphite.
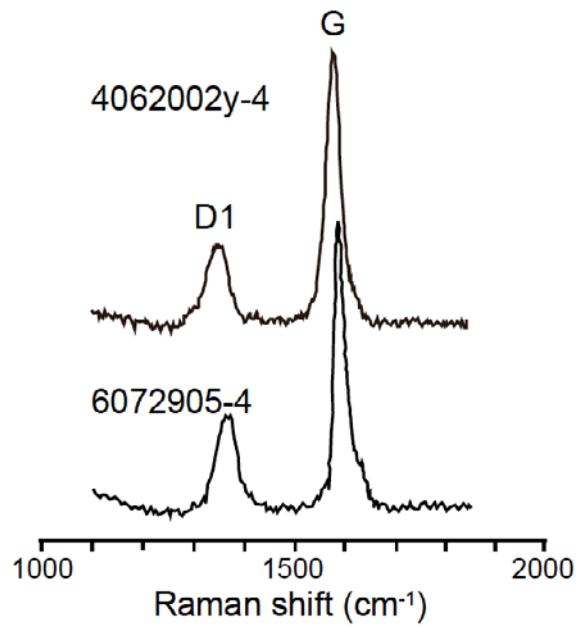
**Figure S4 | Raman spectra of samples 4062002y-4 (from a carbonate vein) and 6072905-4 (from a graphite-rich schist)**. Data sets for each sample are summarized in Supplementary Table S5.
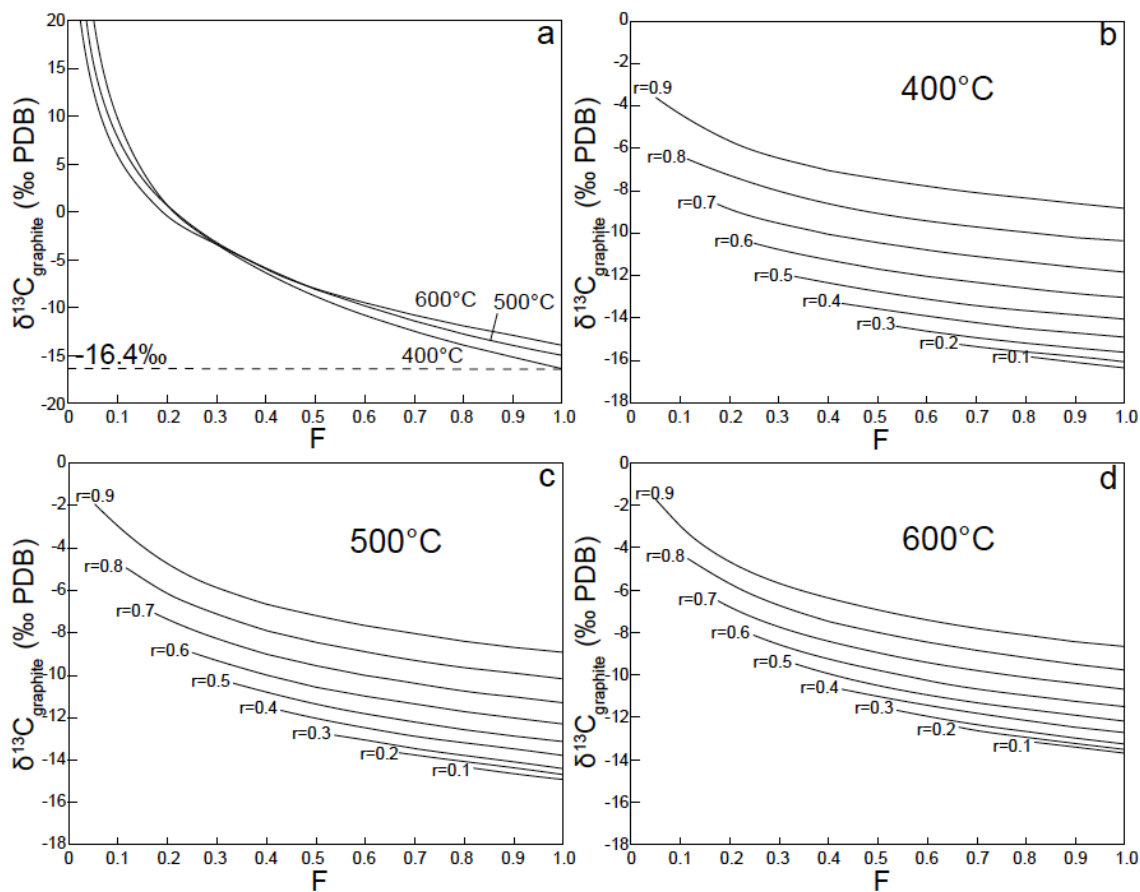
**Figure S5 | Calculation of δ$^{13}$C values for graphite precipitated from metamorphic fluids. a**, Plots of δ$^{13}$C values of graphite precipitated from $CO_2$ by Rayleigh isotopic fractionation at 400°C, 500°C, and 600°C. **b–d**, Plots of δ$^{13}$C values of graphite precipitated from $CO_2$–$CH_4$ fluid by Rayleigh isotopic fractionation at 400°C, 500°C, and 600°C. F = fraction of remaining carbon in the source. r = ratio of the initial number of moles of $CH_4$ and $CO_2$.
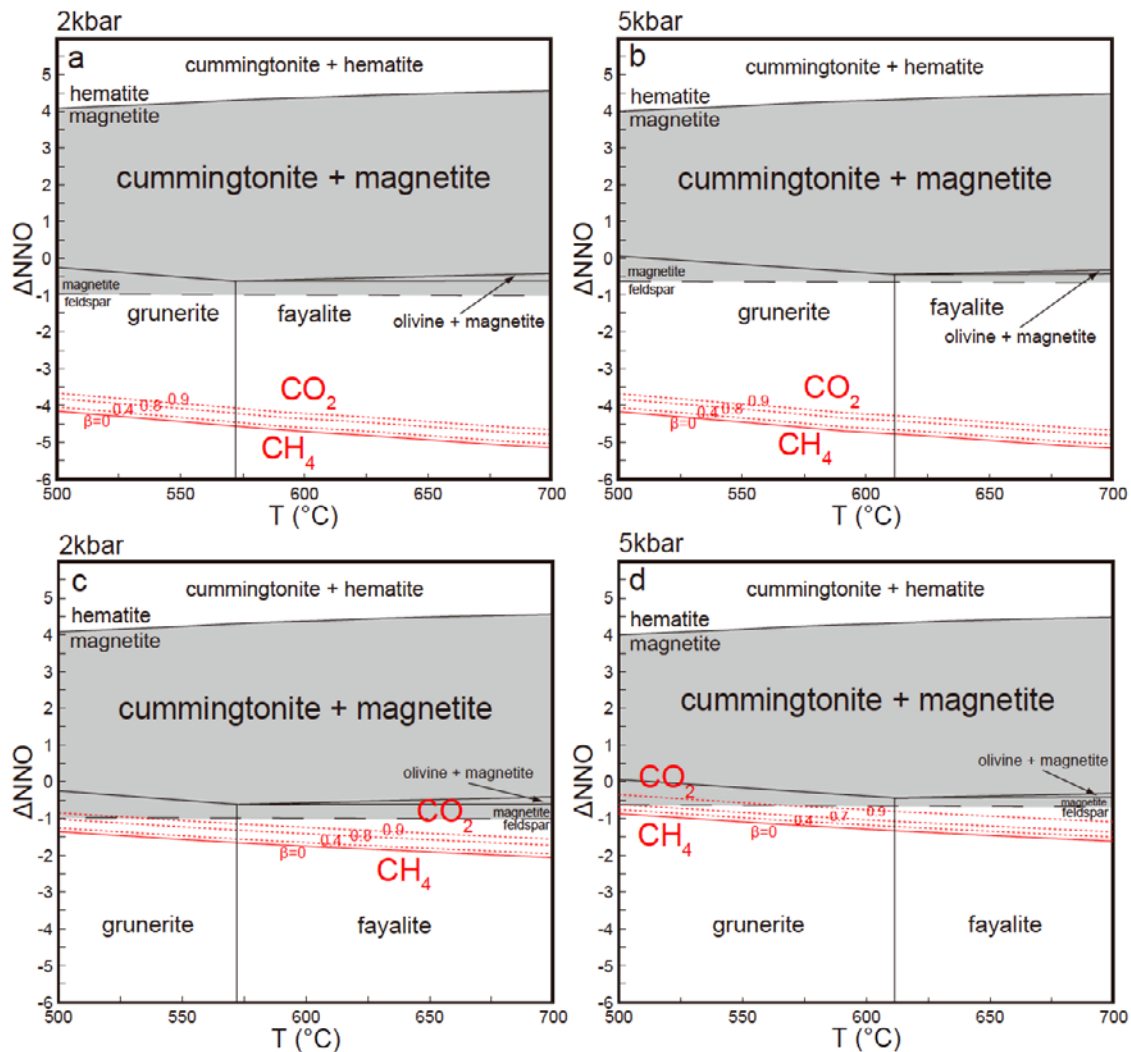
**Figure S6 | Phase diagrams of cummingtonite/grunerite–magnetite, $CO_2$, and $CH_4$ on a ΔNNO–temperature (°C) diagram**. **a** and **b**, Phase diagrams at 2 and 5 kbar, respectively, calculated using the logK values of Ohmoto & Kerrick[27]. **c** and **d**, Phase diagrams at 2 and 5 kbar, respectively, calculated using logK values estimated by SPUCRT92. $β = 1 − f_{CH4}/f_{CO2}$. ΔNNO is defined as the difference between the logarithm of oxygen fugacity and that of the nickel–nickel oxide buffer condition. The grey zone shows the possible redox state of the metamorphic fluid at equilibrium with the surrounding BIFs.

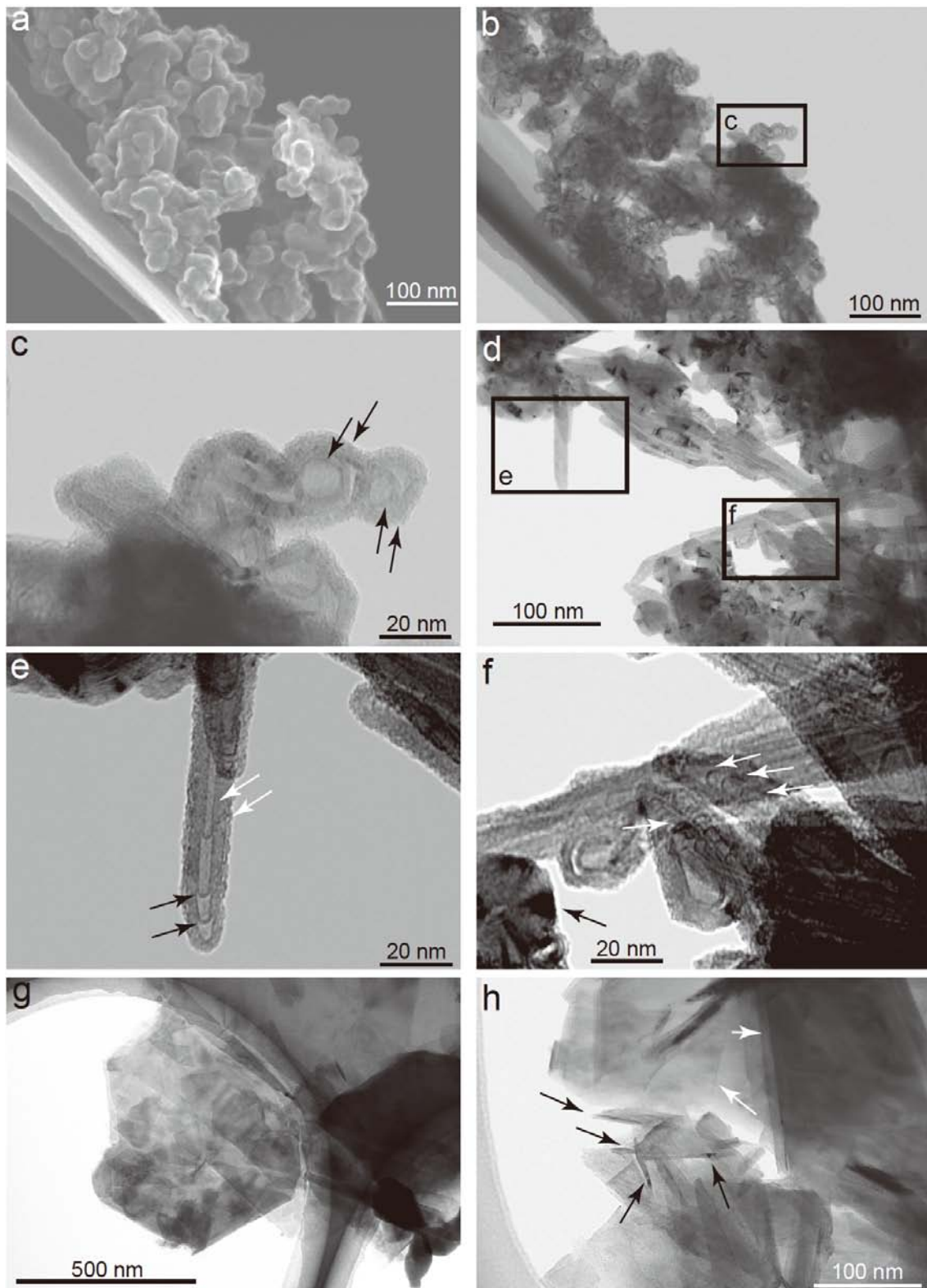**Figure S7 | Scanning transmission electron microscope (STEM) images of graphite from graphite-rich schist (sample 6072906) and a secondary carbonate vein (sample 4062002y). a**, SEM image of graphite grains in sample 6072906, showing that several grains are aggregated together. **b**, TEM

image of the sample shown in panel **a**, taken in bright field emission mode. Panels **a** and **b** demonstrate the benefits of STEM imaging, which can provide SEM and TEM images from the same sample. **c**, Magnification TEM image of the area marked 'c' in panel **b** (bright field image). Individual graphite grains are apparently multi-walled and surrounded by several nanolayers (see black arrows). Individual grains are hexagon shaped. **d**, TEM image of graphite (bright field image) in sample 6072906. Polygonal grains and tube-like structures are visible in the image, which was taken in dark field emission mode. Magnified views of the areas labelled 'e' and 'f' are shown in panels **e** and **f**, respectively. **e**, Multi-walled tubes are visible in this bright field image (white arrows). The interiors of the tubes are separated into compartments (black arrows). **f**, Complex of tube-like structures and polygonal grains. Polygonal grains show colour contrasts within a single grain (black arrow), indicating structural heterogeneity in a single grain. "Rounded" or "bent" tubes (white arrows) are attached to the straight tubes. The walls of the "rounded" and straight tubes are both approximately 5–10 nm thick. **g**, TEM image of graphite (bright field image) from a secondary carbonate vein (sample 4062002y). Well-facetted graphite grains are aggregated together. **h**, TEM image of graphite (bright field image) from a secondary carbonate vein (sample 4062002y). Large graphite flakes (100–300 nm in length) are visible on the right-hand side (white arrows). Small "needle"-like flakes (10–100 nm in length) show composite structures (black arrows).
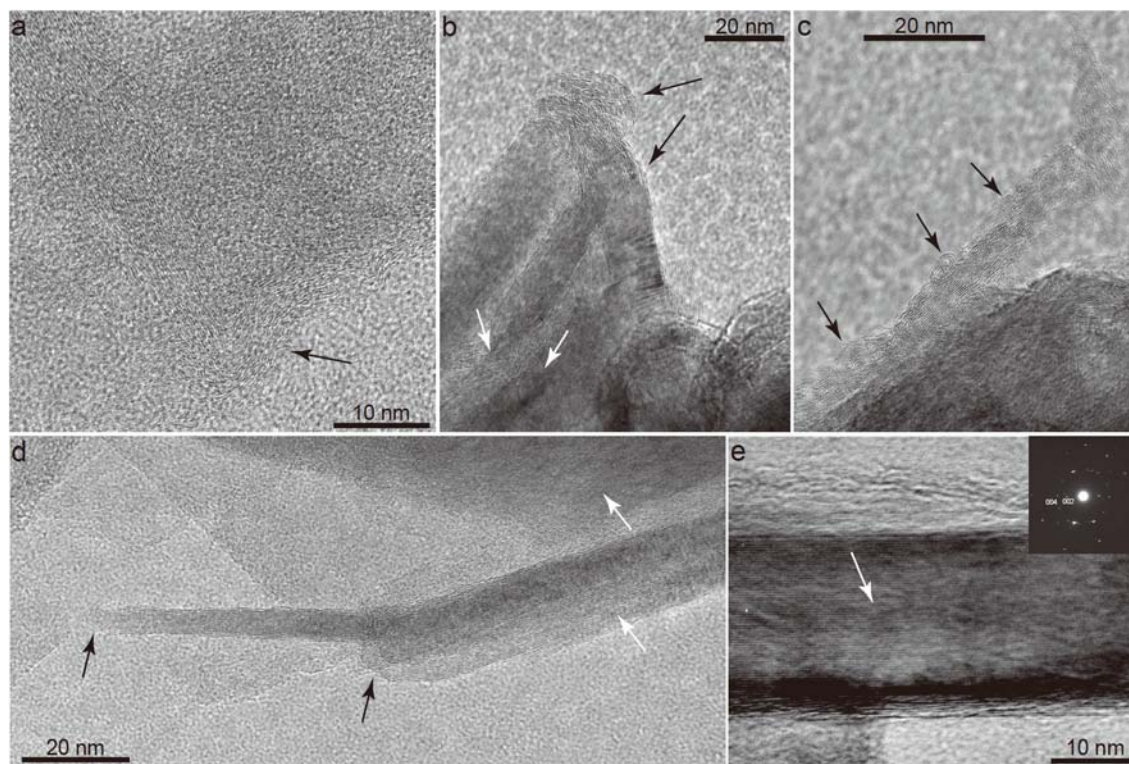
**Figure S8 | High-resolution transmission electron microscope (HRTEM) images of graphite samples**. **a**, HRTEM images of graphite in graphite-rich schist (sample 6072905, from sedimentary graphite). A carbon-free germanium micro-grid was used to obtain this image. This is the same sample as shown in Figure. 4c, which was obtained using a normal Cu-based micro-grid. The image verifies that "onion"-like or distorted structures observed in this study are not an artefact of electron beam attack on carbon in the micro-grid (see black arrow). **b**, HRTEM image of graphite in sample 6072905 (sedimentary graphite). Distorted structures are common at the edges of graphite grains (black arrows). The distorted structures are often visible on the interiors of graphite grains (white arrows). **c**, HRTEM image of graphite in sample 6072906 (sedimentary graphite). Distorted structures are commonly observed on the surfaces of graphite grains. Black arrows indicate rolled and curled structures. **d**, HRTEM images of graphite in sample 4062002y (secondary graphite). In general, well-layered structures are visible (white arrows) on the interiors of graphite flakes. Distorted and curled structures are also visible, but are limited to the edges or surfaces of graphite flakes (black arrows). **e**, HRTEM images of graphite in sample 4062002y (secondary graphite). The interiors of graphite grains show ordered structures with minor bending and distortion (white arrow). The inset at higher right shows the SAED, which was obtained from the same area as that in Supplementary Figure S8**e**. <001>* streaks are unclear, suggesting a dominance of 2H-type stacking.
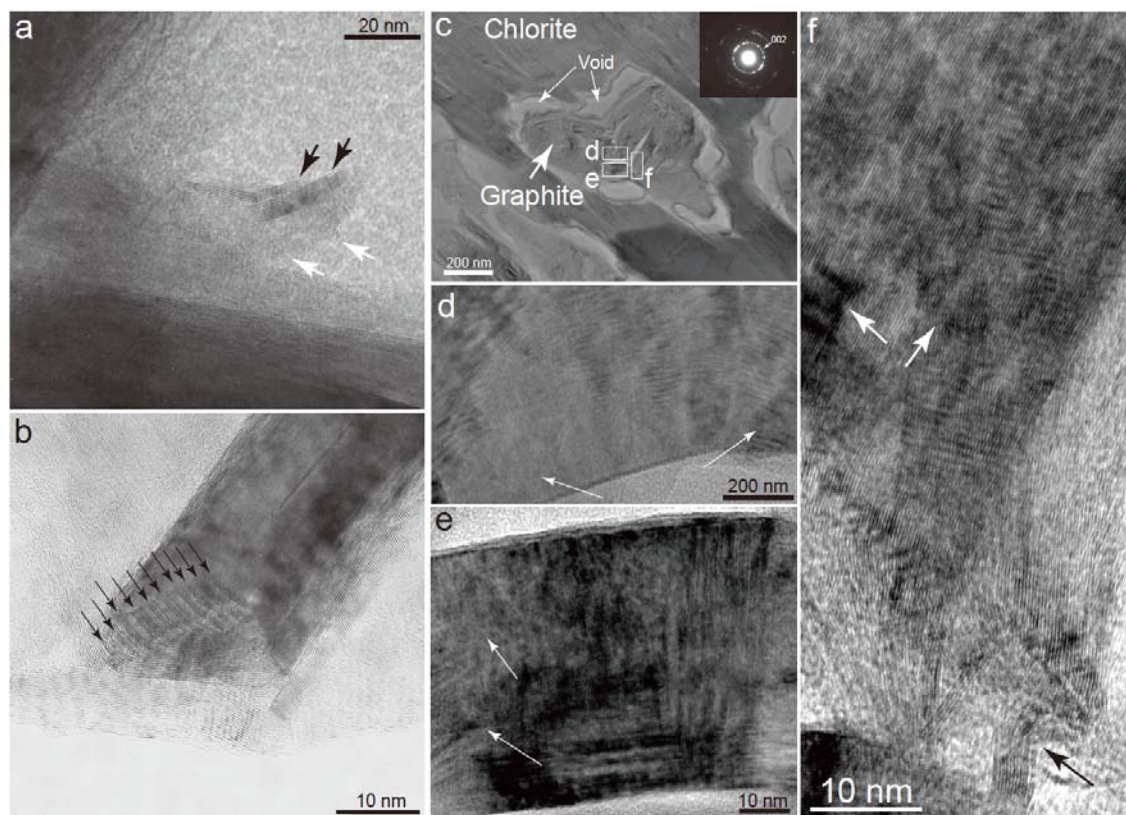
**Figure S9 | HRTEM images of graphite in sample 4062709, 4062710 (southern section) and sample 6072905 (northern section). a**, HRTEM image of graphite in sample 4062709. Overall, sheet-like structures dominate the image (black arrows). Onion-like structures are also visible (white arrows). **b**, HRTEM image of graphite in sample 4062710. Multi-walled layers are evident on the surfaces of graphite grains (black arrows). **c**, TEM image of chlorite and graphite in sample 6072905. A thin rock film of sample 6072905 was attached to a micro-grid and then cut by Ar-ion milling to a size suitable for TEM observation. The size of the cut area is approximately 20 mm$^2$. Some chlorite contains inclusions of graphite. Void space is present at grain boundaries between graphite and chlorite. Graphite inclusions in chlorite appear as aggregated grains. The inset at higher right shows the SAED, which was obtained from the same area as that at the central part (aggregated graphite grains) of Supplementary Figure S9**c**, indicating their turbostratic structure. **d**, TEM image of the area labelled 'd' in panel **c**. Layered structures are visible, indicating an ordered structure. However, graphene layers are bent at the right and left corners (white arrows). **e**, TEM image of the area labelled 'e' in panel **c**. In this image, we interpret that several overlapping grains are present. However, some parts show clear layering of graphane (white arrows). **f**, HRTEM image of graphite. This image was obtained just to the right of the area marked 'f' in panel **c**. Several grains are overlapping in this image, causing moirée effects (the particularly wavy parts of the upper figure) (white arrows). Rolled or "onion"-like structures are present in the lower part of the image

(black arrow). Overall, The effect of silicate to accelerate graphitization, such as variable crystallinity in the vicinity of chlorite, was not observed in the examined samples treated by Ar-ion milling.

Table S1 | Mineral assemblages of typical graphite-rich schists.

| Sample | Quartz | Cummingtonite/Anthophilite | Chlorite | Graphite | Additional Minerals | Structure |
|---|---|---|---|---|---|---|
| Northern section | | | | | | |
| 3072303 | × | × | × | × | apatite, illmenite, zircon, monazite | fine laminations |
| 4062306 | × | × | × | × | apatite | fine laminations |
| 4062307 | × | × | × | × | apatite | fine laminations |
| 4062308 | × | × | × | × | apatite | fine laminations |
| 4062309 | × | × | × | × | apatite | fine laminations |
| 5080501 | | × | | × | | fine laminations |
| 5080502 | | × | | × | | fine laminations |
| 5080503 | | × | | × | | fine laminations |
| 6072905 | × | × | × | × | apatite, illmenite, zircon, monazite | fine laminations |
| 6072906 | × | × | × | × | | fine laminations |
| Central section | | | | | | |
| 4062611 | × | × | × | × | | no structure |
| Southern section | | | | | | |
| 4062709 | × | × | × | × | illmenite | coarse laminations |
| 4062710 | × | × | × | × | | no structure |
| 5080401 | × | × | × | × | | no structure |
| 5080402 | × | × | × | × | | no structure |
| 5080603 | × | × | × | × | illmenite | coarse laminations |

Table S4 | Lattice spacings and full width at half maximum (FWHM) of the examined graphite, determined using XRD analysis.

| Sample | 002 Peak | | 004 Peak | |
|---|---|---|---|---|
| | d (Å) | FWHM (Δθ) | d (Å) | FWHM (Δθ) |
| synthetic graphite | 3.386 ± 0.001 | 0.224 | 1.685 ± 0.001 | 0.321 |
| graphite in metacarbonate vein | 3.385 ± 0.001 | 0.212 | 1.684 ± 0.001 | 0.304 |
| 3072303 | 3.390 ± 0.001 | 0.311 | 1.685 ± 0.001 | 0.412 |
| 4062308 | 3.385 ± 0.001 | 0.309 | 1.684 ± 0.001 | 0.766 |
| 4062307 | 3.391 ± 0.001 | 0.352 | 1.686 ± 0.001 | 0.461 |

Table S5 | Dataset of Raman microspectroscopies of graphite in samples 4062002y and 6072905.

| Sample | Raman shift (cm⁻¹) | | | Height | | | FWHM | | | Peak area | | | R1 (D1/G height ratio) | R2 (D1/(G+D1+D2) area ratio) | Estimated temperature (°C) |
|---|---|---|---|---|---|---|---|---|---|---|---|---|---|---|---|
| | G | D1 | D2 | G | D1 | D2 | G | D1 | D2 | G | D1 | D2 | | | |
| 6072905-1 | 1582 | 1357 | 1617 | 434 | 128 | 75 | 26 | 52 | 20 | 62131.7 | 23443.3 | 4087.6 | 0.296 | 0.26 | 524 |
| 6072905-2 | 1585 | 1358 | 1615 | 451 | 157 | 77 | 26 | 48 | 28 | 52622.6 | 20580.3 | 2725.0 | 0.348 | 0.27 | 520 |
| 6072905-3 | 1587 | 1361 | 1621 | 461 | 155 | 62 | 28 | 50 | 30 | 86412.6 | 29970.1 | 3406.3 | 0.335 | 0.25 | 529 |
| 6072905-4 | 1581 | 1355 | 1613 | 1055 | 264 | 100 | 24 | 50 | 22 | 54258.7 | 19676.5 | 2767.6 | 0.250 | 0.26 | 526 |
| Average | 1584 | 1358 | 1617 | 600 | 176 | 78 | 26 | 50 | 25 | 63856.4 | 23417.6 | 3246.6 | 0.307 | 0.26 | 525 |
| 4062002y-1 | 1578 | 1351 | 1612 | 633 | 115 | 40 | 26 | 52 | 34 | 38826.7 | 20657.3 | 4215.3 | 0.182 | 0.32 | 497 |
| 4062002y-2 | 1580 | 1352 | 1618 | 988 | 220 | 60 | 24 | 50 | 32 | 25589.6 | 14194.3 | 3173.9 | 0.223 | 0.33 | 494 |
| 4062002y-3 | 1584 | 1356 | 1620 | 687 | 179 | 40 | 34 | 54 | 32 | 27872.3 | 16023.7 | 4574.2 | 0.260 | 0.33 | 494 |
| 4062002y-4 | 1581 | 1355 | 1614 | 1230 | 271 | 50 | 26 | 52 | 32 | 31531.1 | 16466.5 | 3984.0 | 0.220 | 0.32 | 500 |
| Average | 1581 | 1354 | 1616 | 885 | 196 | 48 | 28 | 52 | 33 | 30954.9 | 16835.5 | 3986.8 | 0.221 | 0.33 | 496 |

**Supplementary Methods**

*Extraction of reduced carbon and analysis of carbon concentrations*

Analyses of reduced carbon were performed at Tohoku University, Sendai, Japan, using an elemental analyser (EA) (EA1108, Carlo-Erba, Milano, Italy). The powdered rock samples were prepared by crushing rock chips. Samples of rock powder (0.1–0.3 g) were decarbonated in 6 N HCl at 70°C for 12 h. Some HCl-treated samples were further treated with HCl:HF:$H_2O$ (1:4:4 v/v/v in 6 N HCl) at 70°C for approximately 1 week. The acid-treated samples were neutralized by washing several times in ultrapure water. Approximately 10 mg of dried powder was packed into a Sn capsule and placed in the EA1108. Results are presented as chromatograms. Calibration curves were constructed from the peak areas of the standard 2,5-bis-(5-tert-butyl-2-benzoxazol-2-yl) thiophene (BBOT). Carbon concentrations were corrected using the BBOT calibration curve. The limit of detection for the analytical method is approximately 0.01 wt% carbon and the reproducibility of the carbon content is better than 0.01 wt%. Note that if the samples are carbonate-rich, the method has difficulty analysing the carbon isotope compositions of the graphite alone.

*Carbon stable isotope analyses*

HCl-treated and HCl–HF-treated sample powders were placed in a Sn capsule. The sample size for each analysis was in the range of 2–30 μg. The capsules were totally combusted to $CO_2$ in a furnace at 1000°C. The gas sample was then directly transported to a mass spectrometer (MAT252, Finnigan, Thermo, Massachusetts, USA) by a He carrier gas (through a ConFloIII interface; Thermo, Massachusetts, USA). The mass spectrometer analysed the ratios of compounds with masses of 44, 45, and 46. Carbon isotope ratios were expressed in delta notation, as follows:

$$\delta^{13}C\ (‰) = 1000\{(^{13}C/^{12}C)_{sample}/(^{13}C/^{12}C)_{PDB} - 1\},$$

where PDB is the international Pee Dee Belemnite standard. The reproducibility and accuracy of this method, as assessed with various working standards, were within ±0.2‰.

The neodymium–yttrium aluminium garnet (Nd-YAG) laser microprobe analyses were performed to measure carbon stable isotope compositions of a single rock chip (10 × 5 × 0.5 mm). Analytical details were described in a previous study[30]. We measured $C_{carbonate}$ concentrations in the examined samples (Supplementary Table S3) using an EA and confirmed that the samples did not initially include carbonate. The rock chips of the graphite-rich schist were HCl-treated in a Teflon beaker at 100°C for two days to remove trace amounts of carbonate. Acid-treated rock chips were washed several times using ultrapure

water and then dried. Therefore, the effects of $\delta^{13}C_{carbonate}$ can be ignored, although ablation by the laser might reach the interiors of the examined samples.

Rock chips were combusted for 4–5 seconds using a Nd-YAG laser in $TEM_{00}$ mode (wavelength, 1.064 μm; beam diameter, ~25 μm; working standard, graphite rod). The chamber was filled with $O_2$ (~8–20 torr) to convert all graphite to $CO_2$. Each sample of $CO_2$ gas was purified cryogenically through several line traps en route to the mass spectrometer. The typical crater diameter and pit depth created by the laser beam were 50–100 μm and 100 μm, respectively. Gasses generated from one to six laser craters were utilized for a single analysis. Liu et al. (2000)[30] confirmed that the effects of the oxygen-bearing minerals, such as quartz and silicates, on the analysis (the matrix effect) could be ignored by measuring the silica–graphite mixture in the samples. Repeated analyses of a standard graphite rod indicated that the reproducibility and accuracy of the method are within ±0.2‰.

### Major and trace element concentrations

Major and trace element concentrations were determined commercially (Activation Lab, 1336 Sandhill Drive, Ancaster, Ontario, Canada) using inductively coupled plasma–mass spectrometry (ICP–MS). All analyses were performed under research-quality conditions.

### X-ray diffraction analyses

Reduced carbon powders (~0.2 g), purified by the HCl–HF treatment, were placed on a non-reflective sample holder and analysed by X-ray diffraction (XRD, Philips X'pert PRO, PANalycal, Almelo, Netherlands). Synthesized graphite (powder < 100 mesh; >99.99% pure; Sigma-Aldrich Co.) was also analysed with the samples for comparison.

### Raman microspectroscopy

Confocal laser Raman microspectroscopy was performed on graphite using an NRS-5100 device (JASCO, Tokyo, Japan). The diameter of the laser diode, input power, delivered power to the sample surface, and acquisition time for each spectrum were 531.92 nm, 50 mW, 3.3 mW, and 30 seconds, respectively. Peak position, band area (i.e., integrated area), full width at half maximum (FWHM), and Gaussian fittings of bands were determined using NRS-5100 software provided with the microspectroscope. Graphite powder (~50 mg), purified by the HCl–HF treatment, was placed on a glass slide within a 3 × 3 mm area (approximately 0.5 to 1.0 mm in thickness); each sample was analysed four times.

*Scanning transmission electron microscope observations*

Graphite grains were characterized using a scanning transmission electron microscope (STEM) (S5500, Hitachi, Tokyo, Japan; 30 kV). The graphite powders, purified by the HCl–HF treatment, were suspended in ethanol by ultrasonication. The supernatant was dropped onto carbon-free germanium grids (100 mesh). These samples were also used for high-resolution TEM (HRTEM) observations.

*High-resolution transmission electron microscope observations*

The graphite samples for HRTEM analysis were prepared by Ar-ion milling and dropped onto micro-grids. The thin films for the analysis were ground from a thin section mounted on a micro-grid and milled with an Ar-ion beam. An HRTEM (JEOL JEM-2010, Tokyo, Japan; with an accelerating voltage of 200 KeV; or JOEL JEM200CX, Tokyo, Japan; with an accelerating voltage of 300 KeV) was used to observe the lattice of the graphite. Lattice images and selected-area electron diffractions (SAEDs), used to examine partial diffraction patterns for areas of <1 μm in diameter, were obtained with the HRTEM. The SAEDs were obtained using the JEM-2010 with an accelerating voltage of 200 KeV. The scanned area used to obtain a single SAED was approximately 400 × 400 nm.

We did not describe the Ar-ion milling method in the main discussion because of the difficulty of observing lattices in the vertical *c*-axis direction in graphite. Some TEM images obtained on samples prepared by the Ar-ion milling method are shown in the supplementary figures for comparison. Milling using a focused ion beam (FIB) was not adopted in this study on account of the damage caused by the FIB in graphite, which largely degrades the original structure.

**References**

25. Beyssac, O., Goffe, B., Chopin, C. & Rouzaud, J. N. Raman spectra of carbonaceous material in metasediments: a new geothermometer. *J. Metamorph. Geol*. **20**, 859–871 (2002).

26. Horita, J. Carbon isotope exchange in the system $CO_2$-$CH_4$ at elevated temperatures. *Geochim. Cosmochim. Acta* **65**, 1907–1919 (2001).

27. Ohmoto, H. & Kerrick, D. Devolatilization equilibria in graphitic systems. *Am. J. Sci.* **277**, 1013–1044 (1977).

28. Evans, B. W. & Ghiorso, M. S. Thermodynamics and petrology of cummingtonite. *Am. Mineral.* **80**, 649–663 (1995).

29. Comert, H. & Pratt, J. N. The standard molar Gibbs free energy of formation of NiO from high-temperature e.m.f. measurements. *J. Chem. Thermodyn.* **16**, 1145–1148 (1984).

30. Liu, Y., Naraoka, H., Hayashi, K. & Ohmoto, H. Laser microprobe technique for stable carbon isotope analyses of organic carbon in sedimentary rocks. *Geochem. J.* **34**, 195–205 (2000).